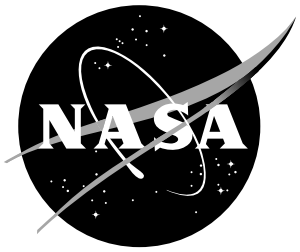

NASA Technical Paper 3589

High Pressure Oxidizer Turbopump (HPOTP) Inducer Dynamic Design Environment

D.A. Herda and R.S. Gross

November 1995

NASA Technical Paper 3589

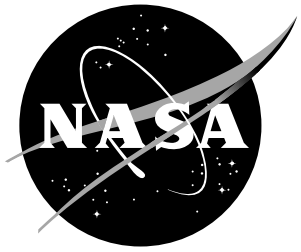

High Pressure Oxidizer Turbopump (HPOTP) Inducer Dynamic Design Environment

D.A. Herda
Marshall Space Flight Center • MSFC, Alabama

R.S. Gross
Auburn University • Auburn, Alabama

National Aeronautics and Space Administration
Marshall Space Flight Center • MSFC, Alabama 35812

November 1995

TABLE OF CONTENTS

LIST OF ILLUSTRATIONS

LIST OF TABLES

TECHNICAL PAPER

HIGH PRESSURE OXIDIZER TURBOPUMP INDUCER DYNAMIC DESIGN ENVIRONMENT

I. INTRODUCTION

Marshall Space Flight Center (MSFC) has historically been involved with the design and development of high pressure oxygen turbopumps (HPOTP's) as part of liquid rocket engine systems. This report focuses on the inducer design methodology. The HPOTP inducer design criteria must include an assumption for the flow-induced dynamic load environment. Vibratory loads are required to perform high cycle fatigue (HCF) and fracture mechanics analyses on the inducer blades. The dynamic loads are a major driver in the inducer design. Over the years, the dynamic load assumptions have been based on "good engineering judgment" and hardware failures. The purpose of this report is to determine realistic inducer dynamic load values for design. This will be accomplished by literature research, evaluation of space shuttle main engine (SSME) criteria, and inducer testing performed at the MSFC inducer test loop (ITL). The technology utilized here may also be applied to other pump and impeller applications.

II. BACKGROUND

The alternate turbopump (AT) HPOTP inducer was tested in the ITL water-flow rig. The AT HPOTP is a new design for the SSME. The AT contains fewer welds and stronger bearings and requires less maintenance than the original SSME HPOTP. The pump contains two inducers (fig. 1). The inducers each have four blades and are unshrouded (fig. 2). The inducers increase the liquid oxygen pressure prior to entering the main impeller. The main impeller in turn increases the fluid pressure to the level required for the main injectors. The inducers contribute 30 percent of the total pressure increase and the main impeller is responsible for 70 percent.

To determine if HCF life requirements are met for the inducer blades, both steady and dynamic stresses are needed. The AT program uses a modified Goodman approach to perform the HCF life analysis. Reference 1 outlines the AT HCF methodology. Steady stresses can be determined analytically by using a computational fluid dynamics model to determine the steady pressure profile on the blade surface. These pressure loads and the centrifugal acceleration are then input into the structural finite element model (FEM) to determine steady stress. Technology for predicting the dynamic stress does not exist. The high dynamic environment is primarily caused by unsteady flow loads, which includes cavitation.

Based on early rocket engine experience, the SSME program has adopted a "rule-of-thumb" for determining the dynamic stress loads for inducers and impellers. This criteria assumes that the dynamic stress is proportional to the mean pressure stress. The 3-sigma dynamic stress is 30 percent of the peak mean pressure stress. Mean pressure stress is defined as the stress induced on the blade due to steady fluid pressure loads. The 30-percent criteria is based on inducer failures in the 1950's and 1960's.[2] Reference 3 addresses the inducer failure on a J-2 engine. The purpose of the ITL test program is to verify the 30-percent criteria experimentally.

An earlier AT inducer water-flow test was performed by Rockwell International, Rocketdyne Division in 1991. Reference 4 is the final test report. Strain gage results showed dynamic to steady stress ratios in excess of 40 percent. However, there was excessive drift in the steady strain gage readings. Also, only one gage was still functioning at the blade leading edge when the nominal engine inlet condition test was performed. The test did substantiate that inducer blade dynamic loads are high. However, there was insufficient data to determine the magnitude of the dynamic/steady strain ratio.

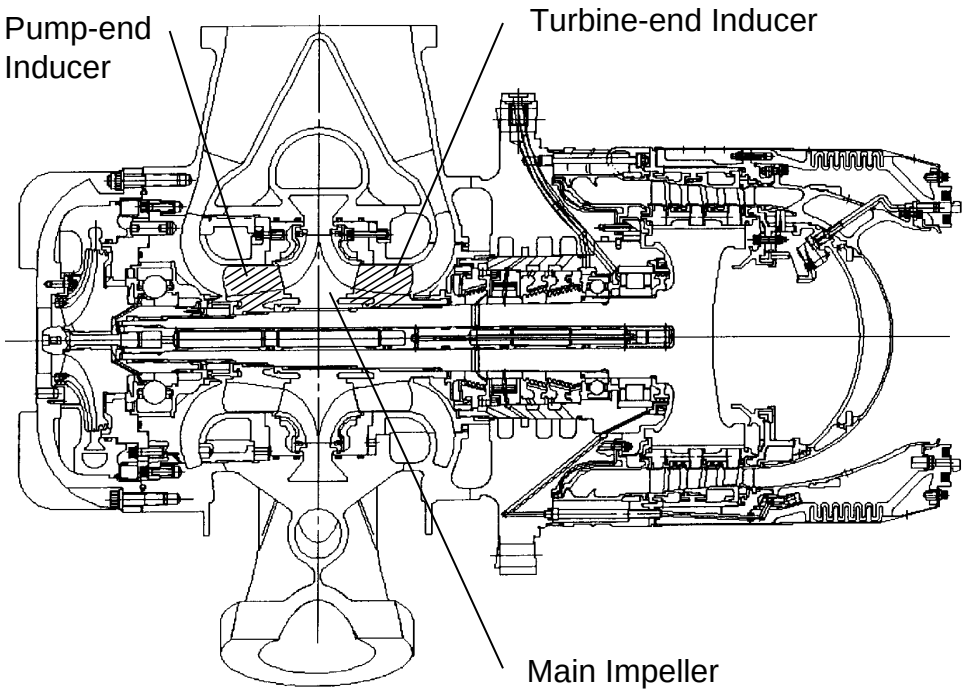

Figure 1. Alternate turbopump HPOTP.

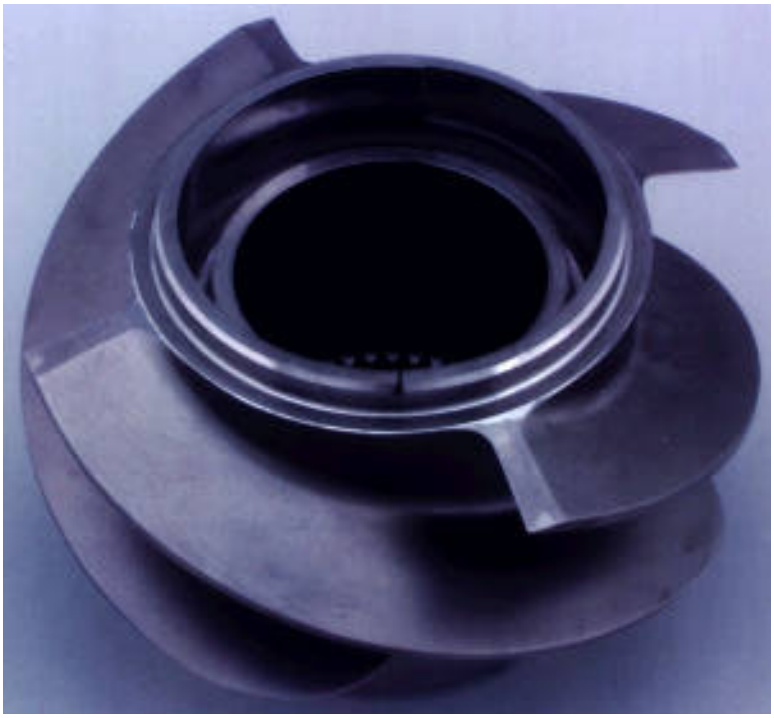

Figure 2. Alternate turbopump HPOTP inducer.

III. TEST PROGRAM

The testing of the AT inducer was performed in the MSFC ITL located in building 4777. The ITL is a closed-loop water-flow system. The test rig is a full-scale model of the SSME AT HPOTP pump inlet. An actual AT configuration inducer was used. The scaling due to differences in the flow parameters (test versus operation) will be discussed in section V.A. Strain gages were mounted on the blades to record both steady and dynamic strain values. The strain gages were electrically connected to the instrumentation via an actively cooled slip ring on the rotating inducer shaft.

Concurrent with the experimental program, an analytical study was developed, which produced a complete NASTRAN FEM of the inducer. The Pratt and Whitney NASTRAN model analysis is discussed in reference 5. Computational fluid dynamics analysis was utilized to determine the blade surface steady pressure loads needed as input to the NASTRAN inducer model. The results of the NASTRAN analysis indicated that for the ITL test conditions, the steady-state blade strains would be very small (<40 μin/in). These low estimates for the strain levels coupled with the hydrodynamic test environment created some stringent conditions on the strain gage installation.

Strain gage locations were determined using the NASTRAN model results. The two-dimensional NASTRAN model consists of the hub and four blades (fig. 3). Figure 4 is a stress contour plot with design operational loads (109-percent rate power level (RPL) service life environment). Gages were placed at the peak stress regions on the blade leading and trailing edges, corresponding to 16- and 82-percent chord length. The other two locations near midchord, 38 percent and 60 percent, were chosen to correspond with positions on the earlier Rocketdyne test.[4]

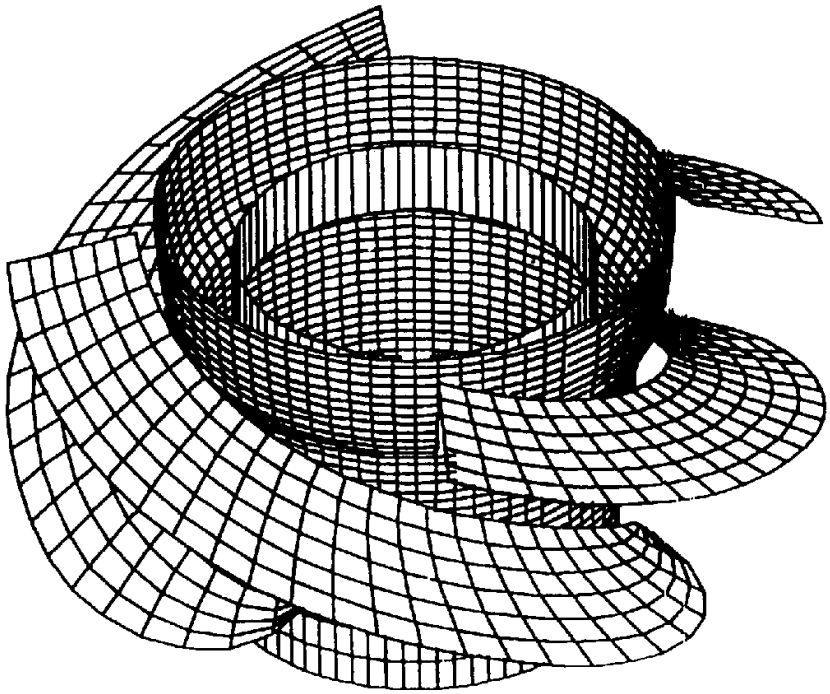

Figure 3. Inducer FEM.

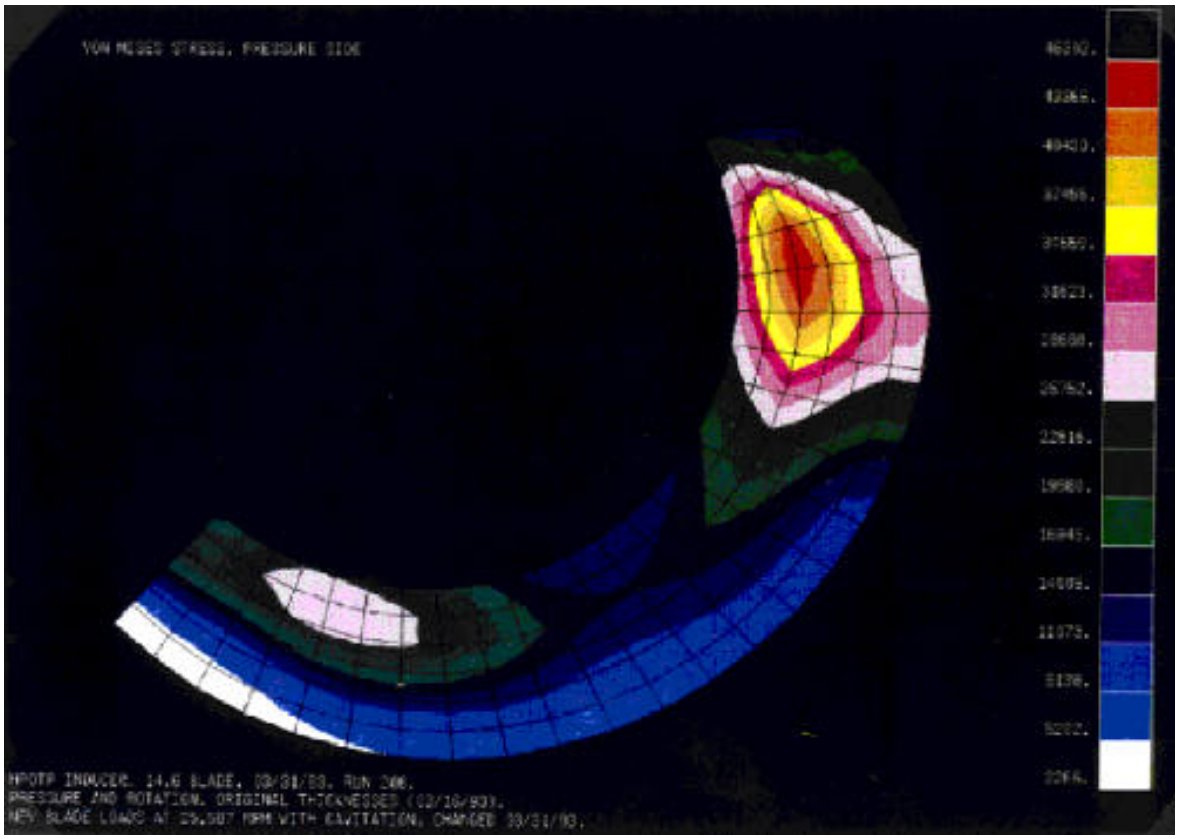

Figure 4. Blade stress contour plot (109-percent RPL).

IV. ANALYSIS/EXPERIMENTAL CORRELATION

The FEM used for the correlation was built by Pratt & Whitney. The correlation was made by comparing model results with strain data taken during the 4,200 r/min dry spin test (no water, centrifugal only). The blades are modeled with one layer of CQUAD4 plate elements. The strain gage recess was represented by reducing the element thickness and offsetting the element centerline. Strain gage pockets in the inducer test hardware are 0.035-in deep. The FEM was run with four different configurations: smooth surface (no recess), 0.020-in recess, 0.035-in recess, and 0.040-in recess. The original purpose of running the four cases was to check sensitivity to pocket depth. Table 1 has the model results for the leading and trailing edge strain gage locations. Figure 5 plots these results. Based on these results, it is apparent that the FEM does not have the fidelity to capture the stress concentration due to the recess.

Table 1. Analytical strain values for the dry spin test (4,200 r/min) blade pressure side.

	Recess Depth			
Location	0.000 in	0.020 in	0.035 in	0.0040 in
Leading Edge	–12.7 μin/in	–10.0	–6.3	–5.0
Trailing Edge	–13.2	–9.7	–5.9	–4.4

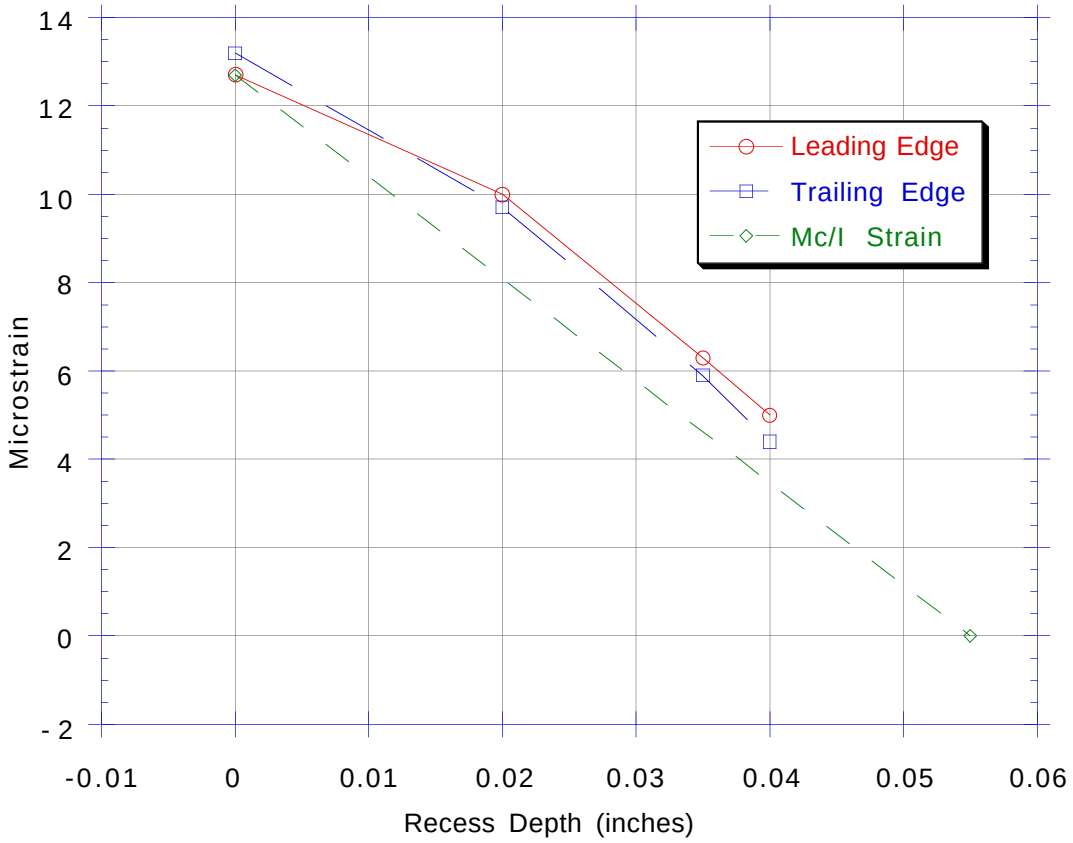

Figure 5. Analytical strain values for the dry spin test.

The strain values predicted by the NASTRAN model are proportional to the distance from the neutral axis to the outer fiber in the recess, i.e., "c" value in bending stress equation. The "Mc/I strain" on the figure represents the strain based on thickness alone.

$$\varepsilon = Mc/EI \quad . \tag{1}$$

Therefore, the model results should be scaled up by the appropriate stress concentration factor (Kt). The Kt was determined using reference 6. The following values were applied to table 37 (case 6b1) in the reference to determine the Kt for a circular hole in a flat plate with out-of-plane bending:

$$r = 0.15 \text{ in} , \quad t = 0.111 \text{ in} , \quad 2r/t = 2.70 \quad .$$

The resulting Kt is 1.96. This value is applied to the model strain values to make the comparison with experimental results. Table 2 shows the comparison of the NASTRAN model results versus the experimental results for the dry spin environment. The model strain values listed are:

$$\varepsilon = \varepsilon_{\text{Radial}} - \varepsilon_{\text{Tangential}} \quad , \tag{2}$$

to be equivalent to the strain gage results. Test results are the average strains recorded from the eleven test dry spin series.

Table 2. Comparison of test versus analytical results for dry spin case.

	$\varepsilon_{Nominal}$ (Model)	ε_{Kt} (Model)	ε (Test)
Leading Edge	–7.4 μin/in	–14.5	–13.5
38-percent Chord	–9.0	–17.7	–16.0
60-percent Chord	–4.5	–8.8	–17.6
Trailing Edge	–6.6	–12.8	–13.5

The ε_{Kt} (Model) includes the 1.96 *Kt* factor. With *Kt* included, the test results compare well with the analysis. All locations are within 10 percent except at the 60-percent chord position. This is excellent correlation considering the small magnitude of the strain values.

V. TEST RESULTS

Sections V.A and V.B address the steady and unsteady test results, respectively. Section V.C determines the strain ratio between unsteady and steady loads to investigate the 30-percent criteria.

A. Steady Strain Results

The finite element analysis predicts a pressure side leading edge strain of 467 μin/in (radial minus tangential strain). This value is for operational loads and needs to be scaled down to the water-flow test environment conditions. Steady pressure loads are a function of fluid density and speed squared. The following equation develops the scale factor (*SF*):

$$SF = \frac{\rho_t \times \omega_t^2}{\rho_a \times \omega_a^2} = 0.0235 \ , \tag{3}$$

where ρ_t = fluid density test (water at 86 $^\circ$F) = 62. lb/ft^3

ρ_a = fluid density analysis (liquid oxygen at –292 $^\circ$F) = 71. lb/ft^3

ω_t = rotational speed test = 4,200 r/min

ω_a = rotational speed analysis = 25,587 r/min .

Including the *Kt* (1.96) and *SF* (0.0235), the analytical strain prediction for the water-flow test on the pressure side leading edge is 21.6 μin/in. Table 3 is a complete list of the predicted versus test strain values. The test strains are taken from run 36/0. This test was run with a low *Nss* value of 5,312 so that cavitation would be minimal. Test 36/0 was chosen to eliminate uncertainties associated with alternate blade cavitation on the leading edges.

Table 3. Comparison of test versus analytical results for engine operation loads (water-flow test environment).

	Analysis	Test
Leading Edge	21.6 μin/in	26.9 μin/in
38-percent Chord	13.3	–6.2
60-percent Chord	16.3	–5.6
Trailing Edge	24.9	–6.5

At the leading edge, the analysis and test strain values correlate well. For the trailing portion of the blade, the analysis over predicts the pressure differential. This is not totally unexpected. The CFD analysis did include cavitation where the test did not. The cavitation assumption increases trailing edge pressure loads by approximately a factor of 2. The test values at 38 percent, 60 percent, and trailing edge appear to be valid since these strains are repeatable and the signal noise is low. Assuming that the test values are correct, delta pressure loads used in the FEM are high by a factor of 3. Figure 6 shows the delta blade pressure used in the analysis.

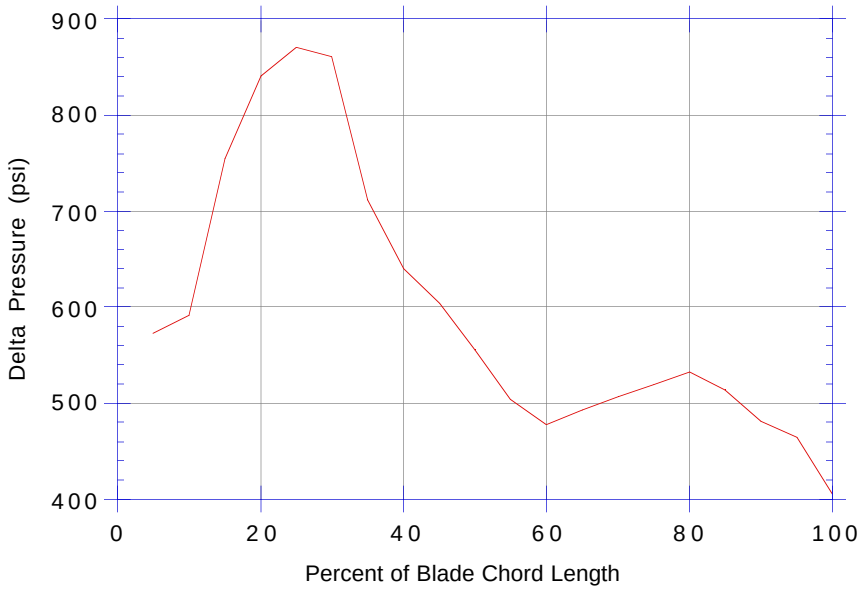

Figure 6. Midspan pressure loads used in finite element analysis.

B. Unsteady Strain Results

Unsteady strain values are taken from test 37/0 (*Nss* = 9,759). This represents nominal engine conditions at both 104- and 109-percent power levels. Figure 7 shows the measured strain values. These are composite strains based on a 2- to 2,000-Hz range. The results listed are for strain gages located on both the pressure and suction surfaces of the blades. Dynamic strain should be similar on both sides. Unsteady strains are greatest at the blade leading edge and decrease toward the trailing edge. The average strain value for the four blades at the leading edge is 4.0 μin/in. This equates to a dynamic stress of 5,100 psi when scaled up to engine level conditions. Therefore, the 3-sigma design value for the AT inducer would be 15,300 psi.

C. Relationship Between Steady and Unsteady Loads

Both values peak near the leading edge and decrease as you move aft. The unsteady stress to steady stress (*US/SS*) ratio actually increases toward the trailing edge due to the low mean pressure stress. The *US/SS* value is determined for each location using test data alone. A simple ratio is set up based on measured strains, and the SF and FEM are not required. The same test conditions utilized in Sections V.A and V.B are used to determine the ratio, i.e., noncavitation for steady pressure loads (test 36/0) and nominal cavitation for the unsteady loads (test 37/0). The steady value is defined as the strain due to pressure only. The pressure-only strain is determined from the test data by subtracting the centrifugal strain component from the combined strain value (Co-CF). This centrifugal force (CF) strain comes directly from the dry spin test data. Table 4 lists the *US/SS* ratios for each chord length position. The strain values shown are the average of the four blades. It would be overly conservative to pick the peak unsteady value and then multiply by three (3-sigma) to determine the design load. The last column shows the 3-sigma design values. Percentages increase significantly at the midchord and trailing edge due to low steady pressure values. However, both the steady and unsteady strains are less than the leading edge at these locations. Therefore, a fatigue analysis performed at the leading edge would envelop the other blade locations.

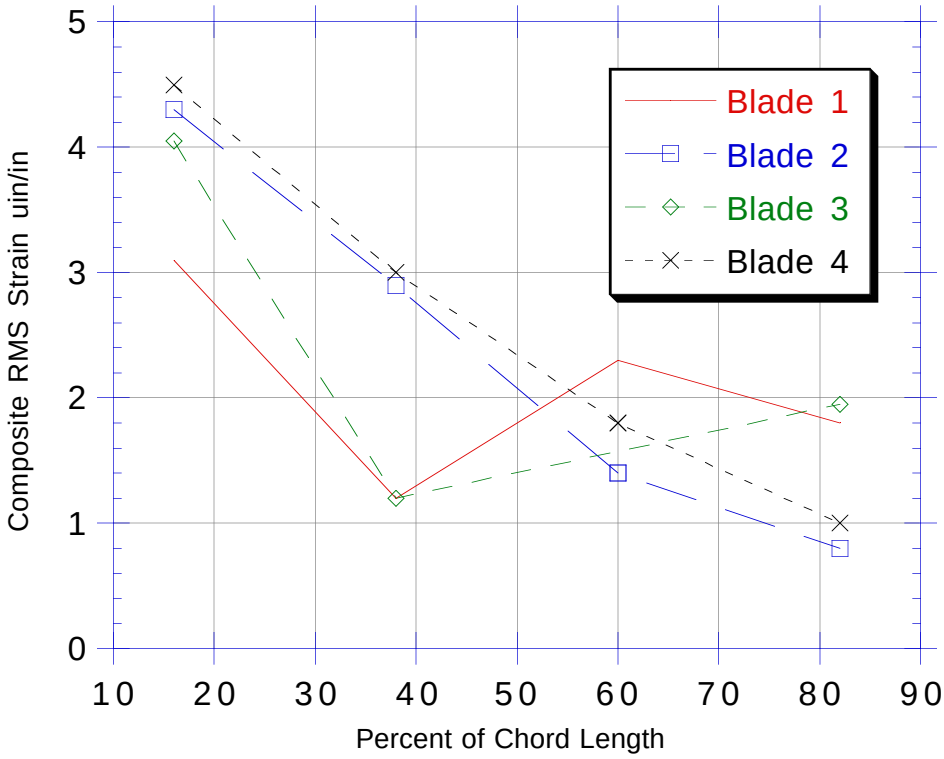

Figure 7. Measured unsteady strains.

Table 4. *US/SS* strain ratios.

Location	Combine Steady (μin/in)	CF Steady (μin/in)	Press Steady (Co-CF) (μin/in)	Unsteady (μin/in)	US/SS (%)	Design (3-sig) *US/SS* (%)
Leading Edge, 16-percent Chord	26.9	–13.8	40.7	4.0	9.8	29.4
38-percent Chord	–6.2	–16.1	9.9	2.1	21.2	63.6
60-percent Chord	–5.6	–17.8	12.2	1.8	14.8	44.4
Trailing Edge. 82-percent Chord	–6.5	–11.9	5.4	1.4	25.9	77.7

VI. CONCLUSIONS

The inducer testing on the MSFC ITL was successful. Strain gage data recorded was of good quality. At the area of concern (blade leading edge), the test data correlate well with the pretest analysis. The assumption that the dynamic stress is 30 percent of the mean pressure stress was verified. The testing determines the ratio to be 29.4 percent at the blade leading edge. The ratios were higher in the lower stressed regions, but the fatigue analysis performed for the leading edge would be the worst case for the inducer. A uniform dynamics stress across the blade, which is 30 percent of the leading edge value, can be assumed to be conservative.

The test demonstrates that inducer/impeller dynamic load levels are tied to the pumping pressure. Moving downstream on the blade surface, both dynamic and steady stress levels decrease. The 30-percent “rule-of-thumb” is a valid assumption to determine 3-sigma dynamic design loads.

For the AT inducer, the dynamic design load is 15.3 ksi. This is based on scaling up the measured strain gage data to the engine operation environment.

REFERENCES

1. Herda, D.A.: “A Comparison of High Cycle Fatigue Methodologies.” NASA TM 103601, August 1992.

2. NASA SP–8052: “Liquid Rocket Engine Turbopump Inducers,” May 1971.

3. Rocketdyne letter SM 0111–7004: “MK 29-F Inducer Failure—Fatigue Sensor Data Analysis,” February 26, 1970.

4. Rockwell International Report RSS–8878: “ATP HPOTP Inducer Water Test Final Report,” January 24, 1992.

5. Pratt and Whitney Report FR–20729–169: “Structural Analysis Report HPOTP Main Impeller and Inducers,” August 1994.

6. Roark, R.J.: “Formulas for Stress and Strain,” Fourth Edition.

7. NASA Memo ED34–18–94: “AT HPOTP Inducer Blade Strain Test (Test No. ITL0006) Pretest Report,” April 4, 1994.

8. NASA Memo ED34–35–94: “ATD HPOTP Water Flow Blade Strain Test Data Reduction,” July 26, 1994.

9. NASTRAN, General Purpose Finite Element Program, Version 67, The MacNeal-Schwendler Corporation, 815 Colorado Blvd., Los Angeles, CA.

APPENDIX A

INSTRUMENTATION

INSTRUMENTATION

The combination of the centrifugal and pressure loading results in both bending and extension (radial and circumferential) of the inducer blades. The two main issues which had to be addressed during the instrumentation selection phase were the low anticipated strain levels and the need to develop a "robust" gage installation capable of surviving the hydrodynamic environment.

To compensate for the low strain levels, semiconductor gages were selected for the majority of the gage locations. The high strain sensitivity of the these gages allowed for the most accurate measurement of the small unsteady (alternating) blade strains, while foil gages were selected to measure the steady-state strain levels. The use of semiconductor gages to measure the steady-state strains was less desirable than the use of foil gages due to the significant thermal shift of the semiconductor gages compared to the foils. The gage thermal shift behavior becomes more critical as the measurement time span increases, as in the case of determination of the steady-state strain levels. Once it was decided to employ both the foil and semiconductor types of gages, the next set of decisions concerned the type of bridge to be employed (quarter, half, or full) and the gage pattern at each of the strain locations.

A full bridge arrangement was selected based on three factors. First, a full bridge provides the highest bridge output compared to the either the quarter or half bridge arrangements. Second, the full bridge provides better temperature compensation. Finally, the slip ring is not in the measurement circuit for the full bridge as opposed to the quarter and half bridge circuits. Once a full bridge arrangement had been selected, the next decision concerned the selection of the gage pattern at each strain location. Two major factors constrained the selection of the gage pattern to a rather limited set of options. The first constraint was the decision to utilize a full bridge arrangement as discussed in the above section which required four active gages at each strain location for effective temperature compensation and bridge completion. The second major constraint arose from the need to recess the gages into the inducer blade to protect the gages from the fluid flow and limit the distortion of the flow pattern over the blade surface during operation. The minimum required depth of the recesses was 0.035 in. This depth allowed for protection of the gages while still providing sufficient room to fill the recess with an epoxy potting compound that could be smoothed to match the blade surface for flow continuity. This minimum recess depth was significant relative to the total blade thickness, which varied from a minimum of 0.090 in to a maximum of 0.170 in. As a consequence, it was not considered structurally advisable to recess both the pressure side (PS) and the suction side (SS) of the blade at the same location.

Given the two constraints, the gage pattern that was selected consisted of two gages mounted radially relative to the rotational axis of the inducer and two gages mounted circumferentially. The Wheatstone bridge wiring results in the following output equation:

$$V_o = \frac{V_i GF(1 - \varepsilon_c / \varepsilon_r)}{[2 / \varepsilon_r + GF(1 + \varepsilon_c / \varepsilon_r)]} \quad , \tag{A-1}$$

where V_o = bridge output voltage,

V_i = input voltage to bridge,

GF = gage factor,

ε_c = circumferential strain,

ε_r = radial strain.

The derivation of equation (A-1) is a rather straightforward procedure starting with the general equation for an unbalanced Wheatstone bridge circuit containing four resistors, R_1, R_2, R_3, and R_4.

Equating R_1 and R_3 to the resistances of the two radial gages (R_r) and setting R_2 and R_4 equal to the resistances of the circumferential gages (R_c) in the general bridge equation results in equation containing R_r and R_c. Finally, relating the change in resistances ΔR_r and ΔR_c to the respective strains, e_r and e_c, leads to equation (A-1). Given the small strain values expected in this test, equation (A-1) was simplified by eliminating the second term in the denominator due to its small magnitude compared with its companion term. The resulting bridge equation becomes:

$$V_o = \frac{V_i GF(1 - \varepsilon_c / \varepsilon_r)}{2 / \varepsilon_r} \quad . \tag{A-2}$$

This equation can be rearranged to yield:

$$\varepsilon_r = \frac{2 V_o}{V_i GF(1 - \varepsilon_c / \varepsilon_r)} \quad . \tag{A-3}$$

The quantities V_i and GF in equation (3) are known prior to the test, and the value of V_o is measured during the test. The two strains, ε_r and ε_c, and the strain ratio, $\varepsilon_c/\varepsilon_r$ are unknown quantities in equation (A-3). Calculation of the absolute strain values required the development of a complimentary equation involving the strains to create a system of two equations with two unknown strains. During the search for this complimentary equation, the authors examined the NASTRAN inducer model to determine the characteristics of the strain ratio $\varepsilon_c/\varepsilon_r$.

Two characteristics of the strain ratio were clearly discernible from the NASTRAN analysis. First, the strain ratio was a significant value relative to 1.0. Therefore, it would be a serious error to eliminate the strain ratio from the term within the denominator in equation (A-3). Second, the strain ratio value was substantially different at different locations on the blade surface, and the ratio values did not correlate well with the Poisson's ratio of the blade material. The authors concluded that the most accurate values available for the strain ratio would be those calculated from the NASTRAN analysis results for each of the gaged locations on the blade. The "analytical" strain ratio values were then employed in equation (1) to calculate the experimental strain ε_r. This procedure of employing an analytical value to facilitate the calculation of experimental strains is certainly not an ideal procedure, but the authors were unable to develop a more appropriate method.

A simple cantilevered beam specimen was produced to examine the validity of this experimental-analytical method for determining the blade strains. Instrumentation of the beam involved the use of a pattern of four foil gages identical to the foil gages employed on the actual inducer. Machining of the specimen, bonding of the gages, and wiring of the bridge were all accomplished by the same organization responsible for the inducer instrumentation. Loading of the beam involved hanging a set of dead weights at the free end. A finite element model of the beam was constructed from CQUAD4 plate elements using MSC/PAL2 to provide the value of the strain ratio $\varepsilon_c/\varepsilon_r$ needed for the calculation of the experimental strains using equation (A-3).

This FEM was employed to allow for the modeling of the strain gage recess machined into the beam. The presence of the recess strongly influences the strain state. This influence became apparent when a finite element model of the beam without the recess (model A) is compared to a model with the recess (model B). Calculation of the axial and transverse strains for model A, 0.035 in below the top surface of the beam (i.e., equivalent recess depth) yields strain values that differ from model B strains by over 74 percent. This comparison of models A and B demonstrates that a significant strain concentration factor occurs due to the presence of the recess which must be accounted for by incorporating the gage recesses into the FEM of the inducer. The experimental and analytical results for the cantilevered beam are listed in table 5.

Table 5. Experimental and analytical strain values for a simple cantilevered beam specimen.

Load	Strain (FE Anal, Model B)			Strain (Experiment)		
(lb)	ε_x ($\mu\varepsilon$)	ε_y ($\mu\varepsilon$)	$\varepsilon_y/\varepsilon_x$[1]	ε_x ($\mu\varepsilon$)	ε_y ($\mu\varepsilon$)	$\varepsilon_y/\varepsilon_x$[1]
1.0	62	–11	–0.17	69	–12	–0.17
2.0	124	–21	–0.17	136	–23	–0.17
3.0	186	–32	–0.17	204	–35	–0.17
4.0	248	–43	–0.17	269	–47	–0.17

Note: 1. The strain ratio was determined by the finite element analysis results. This analytical strain ratio was employed in equation (A-3), along with the experimental bridge output, to produce the experimental strain values listed in table 5.

The data listed in table 5 is significant for two reasons. First, the agreement between the experimental and analytical strain values is quite good (<12-percent difference). Second, the influence of the recess on the strains measured by the gages is accurately represented by the FEM incorporating the recess (model B). In addition, the strain ratio listed in table 5 does not correspond to the magnitude of the Poisson's ratio for the beam material (ν = 0.27). This discrepancy is due to the distortion of the "natural" strain state in the beam by the presence of the recess.

Based on the results of this simple cantilevered beam test case, the FEM of the ATD inducer was modified to incorporate the strain gage recesses. To calculate the radial and circumferential strains from equation (A-3), the values of the strain ratio ($\varepsilon_c/\varepsilon_r$) had to be supplied to the data reduction algorithm via the finite element results. The finite element derived strain ratios are listed in tables 6 and 7 for the 16 gaged locations (four locations per blade). The results listed in table 6 are for the centrifugal loading conditions (dry spin, 4,200 r/min), whereas, the data listed in table 7 are for the 109-percent engine performance condition.

The final section of the data analysis program involved the conversion of the strain results (ε_r and ε_c) determined from equation (A-3) by using the experimental bridge output and the strain ratios from tables 6 and 7. These values, ε_r and ε_c, represent the strains at the bottom of the gage recess. The strains that are needed to predict the high cycle fatigue life of the inducer are those at the blade surface of an unmodified inducer, i.e., one with no machined recesses. The conversion from the measured recess strains to the blade surface strains was accomplished through comparison of the modified (recesses) and unmodified inducer FEM's.

Table 6. Strain ratios calculated at the gage locations for the dry spin (4,200 r/min) condition.

Instrument ID	Blade Number	Blade Surface	Percent Chord	Gage Type	Strain Ratio $\varepsilon_c/\varepsilon_r$
SG-1-PSLE-S	1	Pressure	16	semi	–0.17
SG-1-PS38-S	1	Pressure	38	semi	–0.06
SG-1-PS60-S	1	Pressure	60	semi	0.36
SG-1-PSTE-S	1	Pressure	82	semi	–0.07
SG-2-SSLE-S	2	Suction	16	semi	0.62
SG-2-PS38-S	2	Pressure	38	semi	–0.04
SG-2-PS60-S	2	Pressure	60	semi	0.35
SG-2-SSTE-S	2	Suction	82	semi	0.22
SG-3-PSLE-F	3	Pressure	16	foil	–0.14
SG-3-PS38-S	3	Pressure	38	semi	–0.06
SG-3-PS60-F	3	Pressure	60	foil	0.21
SG-3-PSTE-F	3	Pressure	82	foil	–0.01
SG-4-PSLE-S	4	Pressure	16	semi	–0.17
SG-4-PS38-S	4	Pressure	38	semi	–0.06
SG-4-PS60-F	4	Pressure	60	foil	0.21
SG-4-PSTE-S	4	Pressure	82	semi	–0.07

Table 7. Strain ratios calculated at the gage locations for the 109-percent engine performance condition.

Instrument ID	Blade Number	Blade Surface	Percent Chord	Gage Type	Strain Ratio $\varepsilon_c/\varepsilon_r$
SG-1-PSLE-S	1	Pressure	16	semi	0.53
SG-1-PS38-S	1	Pressure	38	semi	0.47
SG-1-PS60-S	1	Pressure	60	semi	0.24
SG-1-PSTE-S	1	Pressure	82	semi	0.21
SG-2-SSLE-S	2	Suction	16	semi	–0.21
SG-2-PS38-S	2	Pressure	38	semi	0.46
SG-2-PS60-S	2	Pressure	60	semi	0.24
SG-2-SSTE-S	2	Suction	82	semi	1.33
SG-3-PSLE-F	3	Pressure	16	foil	0.30
SG-3-PS38-S	3	Pressure	38	semi	0.47
SG-3-PS60-F	3	Pressure	60	foil	0.15
SG-3-PSTE-F	3	Pressure	82	foil	0.10
SG-4-PSLE-S	4	Pressure	16	semi	0.53
SG-4-PS38-S	4	Pressure	38	semi	0.47
SG-4-PS60-F	4	Pressure	60	foil	0.15
SG-4-PSTE-S	4	Pressure	82	semi	0.21

APPENDIX B

TEST DATA

Dry Spin Test Data (4,200 r/min)
Strain Gauge Results (μin/in)

Test #	1-psle-s	l-ps38-s	1-ps60-s	1-pste-s	2-ssle-s	2-ps38-s	2-ps60-s	2-sste-s	3-psle-f	3-ps38-s	3-ps60-f	3-pste-f	4-psle-s	4-ps38-s	4-ps60-f	4-pste-s
1	–15.04	–16.23	–17.80	–12.95	3.73	–16.89	–16.12	5.28	–15.15	–14.54	–18.76	–17.76	–12.40	–16.66	–19.68	–10.45
2	–14.30	–16.23	–17.23	–13.51	4.83	–16.58	–15.91	6.40	–13.98	–15.09	–17.72	–17.08	–12.20	–16.39	–18.93	–10.63
3	–14.30	–16.28	–17.40	–13.32	4.71	–16.59	–16.21	5.97	–14.23	–15.27	–18.32	–16.84	–12.21	–16.36	–18.97	–10.67
4	–14.28	–16.11	–17.07	–13.29	4.59	–16.69	–15.72	6.35	–14.64	–14.77	–18.16	–17.29	–12.17	–16.25	–19.08	–10.59
5	–14.93	–16.37	–18.28	–13.30	3.47	–17.07	–16.46	4.68	–15.64	–14.84	–19.78	–18.38	–12.07	–16.66	–20.91	–10.77
6	–14.63	–16.17	–17.25	–12.91	4.55	–16.56	–15.99	6.07	–14.95	–14.96	–18.07	–17.03	–12.32	–16.32	–18.94	–10.55
7	–15.09	–16.50	–17.91	–12.97	3.81	–16.99	–16.17	5.03	–15.44	–14.75	–19.02	–17.72	–12.22	–16.51	–19.66	–10.91
8	–14.03	–15.96	–15.95	–12.09	6.01	–16.25	–15.03	6.92	–13.94	–14.34	–17.03	–15.52	–11.96	–15.97	–17.92	–10.70
9	–14.00	–16.11	–15.73	–12.51	5.92	–16.16	–15.19	7.39	–13.42	–14.85	–16.61	–15.39	–12.27	–15.89	–17.98	–11.08
10	–15.63	–16.83	–17.81	–13.08	1.89	–16.74	–15.62	6.65	–¡4.42	–15.18	–18.19	–16.55	–13.79	–16.66	–20.08	–10.89
11	–14.39	–16.70	–16.92	–12.28	3.52	–16.35	–15.35	4.49	–14.16	–14.57	–17.87	–17.18	–12.51	–16.49	–19.41	–10.68
Average	–14.60	–16.32	–17.21	–12.93	4.28	–16.62	–15.80	5.93	–14.54	–14.83	–18.14	–16.97	–12.37	–16.38	–19.23	–10.72

Determination of average values for correlation with analysis

	Blade 1	Blade 2	Blade 3	Blade 4	Average
Pressure side leading edge	–14.60	N/A	–14.54	–12.37	–13.8
Pressure side 38-percent chord	–16.32	–16.62	–14.83	–16.38	–16.0
Pressure side 60-percent chord	–17.21	–15.80	–18.14	–19.41	–17.6
Pressure side trailing edge	–12.93	N/A	–16.97	–10.72	–13.5

N/A – Not applicable, strain gauge on suction side.

Operation Load Conditions
Strain Gauge Results (μin/in)

	Test 36		Test 37		Test 38		Test 39	
Strain Gauge	Steady	Comp. RMS	Steady	Comp. RMS	Steady	Comp. RMS	Steady	Comp. RMS
1-PSLE-S	22.9	2.7	4.6	3.1	5.5	2.4	5.4	2.8
1-PS38-S	–7.3	1.9	–0.2	1.2	–2.8	0.9	–3.7	1.0
1-PS60-S	–6.8	1.0	1.0	2.3	4.1	0.8	3.2	0.8
1-PSTE-S	–6.8	1.1	–4.5	1.8	7.6	2.3	9.2	1.6
2-SSLE-S	–36.9	3.6	–18.4	4.3	–6.8	1.8	–8.8	1.6
2-PS38-S	–7.3	1.8	–8.2	2.9	–13.8	3.5	–14.4	3.5
2-PS60-S	–5.2	1.0	–6.6	1.4	–8.2	2.1	–9.5	2.3
2-SSTE-S	0.6	0.8	–2.5	0.8	–3.1	1.0	–2.9	1.1
3-PSLE-F	34.0	4.3	14.1	4.1	14.6	3.8	13.9	4.3
3-PS38-S	–6.8	1.7	1.0	1.2	–1.9	1.0	–2.9	1.1
3-PS60-F	–5.1	ND	5.0	ND	8.7	ND	7.5	ND
3-PSTE-F	–8.2	1.5	–5.3	2.0	6.6	2.6	9.2	2.2
4-PSLE-S	23.8	3.9	–5.9	4.5	–18.1	1.6	–16.7	1.5
4-PS38-S	–5.2	1.7	–7.5	3.0	–14.0	3.7	–14.6	3.9
4-PS60-F	–5.3	1.7	–8.3	1.8	–9.6	2.1	–10.8	2.3
4-PSTE-S	–4.6	1.0	–3.8	1.0	–3.7	1.2	–4.0	1.3

Test 36 – Noncavitating, Nss = 5,312
Test 37 – Nominal engine cavitation, NSS = 9.759
Test 38 – NSS = 10,889
Test 39 – Nss = 11,521

Operation Load Conditions (Continued)
Strain Gauge Results (μin/in)

Determination of steady strains from test 36

	Blade 1	Blade 2	Blade 3	Blade 4	Average
Pressure side leading edge	22.9	SS	34.0	23.89	26.9
Pressure side 38-percent chord	–7.3	–7.3	–5.1	–5.2	–6.2
Pressure side 60-percent chord	–6.8	–5.2	–5.1	–5.3	–5.6
Pressure side trailing edge	–6.8	SS	–8.2	–4.6	–6.5

Determination of unsteady strains from test 37

	Blade 1	Blade 2	Blade 3	Blade 4	Average
Pressure side leading edge	3.1	4.3	4.1	4.5	4.0
Pressure side 38-percent chord	1.2	2.9	1.2	3.0	2.1
Pressure side 60-percent chord	2.3	1.4	ND	1.8	1.8
Pressure side trailing edge	1.8	0.8	2.0	1.0	1.4

SS – Suction Side
ND – No Data